Microwave Quantum Memristors

X.-Y. Qiu,[1,*] S. Kumar,[2,*] F. A. Cárdenas-López,[3] G. Alvarado Barrios,[2,†] E. Solano,[2] and F. Albarrán-Arriagada[4,5,‡]

[1]*International Center of Quantum Artificial Intelligence for Science and Technology (QuArtist) and Physics Department, Shanghai University, 200444 Shanghai, China*
[2]*Kipu Quantum, Greifswalderstrasse 226, 10405 Berlin, Germany*
[3]*Forschungszentrum Jülich GmbH, Peter Grünberg Institute, Quantum Control (PGI-8), 52425 Jülich, Germany*
[4]*Departamento de Física, Universidad de Santiago de Chile (USACH), Avenida Víctor Jara 3493, 9170124, Santiago, Chile.*
[5]*Center for the Development of Nanoscience and Nanotechnology, 9170124, Estación Central, Chile.*

We propose a design of a superconducting quantum memristive device in the microwave regime, that is, a microwave quantum memristor. It comprises two linked resonators, where the primary one is coupled to a superconducting quantum interference device (SQUID), allowing the adjustment of the resonator properties with an external magnetic flux. The auxiliary resonator is operated through weak measurements, providing feedback to the primary resonator via the SQUID and establishing stable memristive behavior via the external magnetic flux. The device operates with a classical input signal in one cavity while reading the response in the other, serving as a fundamental building block for arrays of microwave quantum memristors. In this sense, we observe that a bipartite setup can retain its memristive behavior while gaining entanglement and quantum correlations. Our findings open the door to the experimental implementation of memristive superconducting quantum devices and arrays of microwave quantum memristors on the path to neuromorphic quantum computing.

I. INTRODUCTION

Neuromorphic computing has emerged as a promising avenue for energy-efficient and advanced computing systems [1], utilizing nonlinear devices with memory properties such as phase-change memory, transistors, spintronic devices, and memristors [2] to achieve heightened computational capabilities. Memristors, as nonlinear resistors, can be well described by Kubo's response theory [3, 4], where one characteristic feature is the pinched hysteresis loop in their input-output relation, which can be associated to memory properties [5]. In 1971, L. Chua introduced the memristor concept as a theoretical fourth fundamental circuit element [6]. Its experimental realization was later confirmed by HP Labs in 2008 [7]. However, the precise existence of the ideal memristor, as postulated by Chua, remains debated [8]. Recently, memristors have been studied as fundamental elements for neuromorphic computing [9–12], offering potential for robust neuromorphic architectures [13–16] beyond von Neumann's architectures [17–19].

On the other hand, quantum computing has shown the potential to revolutionize computer science with the first claims of quantum advantage, but always in the context of von Neumann's architecture. In this context, it is natural to think of quantum memristors, that is, memristors working in the quantum regime. In recent years, quantum memristors have been proposed in platforms like superconducting circuits [20–24] and photonics [25, 26], with an experimental realization in 2021 [27]. These proposals align with the emergence of neuromorphic quantum computing, which aims to develop quantum hardware and software implementations with brain-inspired devices [28–30]. Scalable quantum memristors may also enable the development of analog devices that simulate brain-inspired functions, nonlinear models of materials, biology, and finance. Ongoing studies on coupled quantum memristors have shown the nontrivial presence of quantum correlations in a memristive dynamics, a useful resource for interconnected quantum memristor arrays [31, 32], as is suggested in reservoir computing paradigm [27].

In this work, we propose a superconducting circuit design for the feasible implementation of a microwave quantum memristor and its extension to multipartite arrays. Our proposal employs two coupled LC oscillators and a SQUID to adjust the effective frequency of one of the oscillator through an external magnetic flux. Such external magnetic flux depends on a weak measurement over the other oscillator, thus implementing a feedback process. We characterize the memristive response of the proposed device to the external voltage applied over one of the oscillators. To do this, we consider different separable and entangled initial states. Additionally, we explore the response of coupled devices, computing the quantum correlations during the memristive dynamics, revealing a nontrivial behavior.

II. CLASSICAL AND QUANTUM MEMRISTORS

We characterize a memristive system by its dynamical relation [33]

$$y(t) = g\big[x, u, t\big]u(t), \tag{1}$$

where $y(t)$ and $u(t)$ stand for the output and input signal of the system, respectively, and are related through the response function $g[x, u, t]$. The response function also depends on a state variable x whose dynamics is described by the equation

$$\dot{x} = f\big[x, u, t\big]. \tag{2}$$

In the context of electrical circuits, and specifically for memristors, the response function $g[x, u, t]$ is usually called mem-

* Co-first authors
† phys.gabriel@gmail.com
‡ francisco.albarran@usach.cl

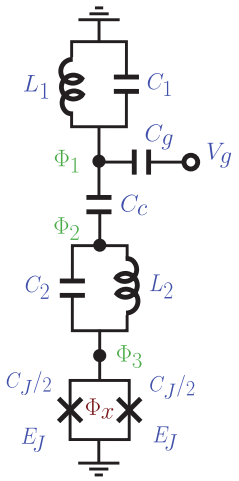

FIG. 1. Circuit design for the proposed memristive device in the microwave regime. The input signal is given by V_g, and the feedback is provided by the magnetic flux Φ_x through the SQUID.

ristance [33, 34] and can be derived using linear response theory developed in 1957 by R. Kubo [35].

Now, we can define a quantum memristor in a similar way. We can consider observables $\langle\hat{y}(t)\rangle$ and $\langle\hat{u}(t)\rangle$ following a similar relation as Eq. (1)

$$\langle\hat{y}(t)\rangle = G\big[\langle\hat{x}\rangle,\langle\hat{u}\rangle,t\big]\langle\hat{u}(t)\rangle, \tag{3a}$$

$$\langle\dot{\hat{x}}\rangle = F\big[\langle\hat{x}\rangle,\langle\hat{u}\rangle,t\big]. \tag{3b}$$

Here, $G\big[\langle\hat{x}\rangle,\langle\hat{u}\rangle,t\big]$ and $F\big[\langle\hat{x}\rangle,\langle\hat{u}\rangle,t\big]$ are the quantum analog to the response and state variable function, respectively.

III. THE MODEL

We consider the circuit shown in Fig. 1, which is composed of two LC oscillators, each with a capacitance C_j and inductance L_j, and coupled by a capacitor C_c. One of the resonators, labeled with $j = 2$, is coupled galvanically to a SQUID, which consists of a closed loop with two Josephson junctions. The SQUID in the circuit acts as a Josephson junction with capacitance C_J and tunable Josephson energy, given by $2E_J|\cos(2\pi\Phi_x/\Phi_0)|$, which depends on the external magnetic flux Φ_x threading the SQUID. Here $\Phi_0 = h/(2e)$ is the superconducting magnetic flux quantum. The role of the SQUID in this design is to change the cavity properties using the external magnetic flux Φ_x as feedback. Finally, we provide an input signal using a voltage source coupled capacitively, as is shown in Fig. 1. The Lagrangian that describes our circuit reads

$$\begin{aligned}\mathcal{L} =& \frac{C_1}{2}\dot{\Phi}_1^2 - \frac{\Phi_1^2}{2L_1} + \frac{C_g}{2}(\dot{\Phi}_1 - V_g)^2 + \frac{C_c}{2}(\dot{\Phi}_1 - \dot{\Phi}_2)^2 \\ &+ \frac{C_2}{2}(\dot{\Phi}_2 - \dot{\Phi}_3)^2 - \frac{(\Phi_2 - \Phi_3)^2}{2L_2} + \frac{C_J}{2}\dot{\Phi}_3^2 \\ &+ 2E_J\cos(\varphi_x)\cos(\varphi_3),\end{aligned} \tag{4}$$

where $\varphi_3 = 2\pi\Phi_3/\Phi_0$ is the superconducting phase and $\varphi_x = 2\pi\Phi_x/\Phi_0$. Using the Legendre transformation and second-quantization techniques, we obtain the system Hamiltonian $\hat{\mathcal{H}}$ as (for detailed derivation, see Appendix A)

$$\begin{aligned}\hat{\mathcal{H}}(\Phi_x) =& \sum_{\ell=1,2}\Big[\omega_\ell(\Phi_x)\hat{a}_\ell^\dagger\hat{a}_\ell + iG_{g_\ell}(\Phi_x,V_g)(\hat{a}_\ell^\dagger - \hat{a}_\ell)\Big] \\ &+\lambda^+(\Phi_x)(\hat{a}_1^\dagger\hat{a}_2 + \hat{a}_1\hat{a}_2^\dagger) + \lambda^-(\Phi_x)(\hat{a}_1^\dagger\hat{a}_2^\dagger + \hat{a}_1\hat{a}_2),\end{aligned} \tag{5}$$

where we adopt the convention $\hbar = 1$. Here, $\omega_\ell(\Phi_x)$ is the effective frequency of the ℓth resonator, modified by the external magnetic signal in the SQUID. The effect of the voltage source V_g over each cavity is represented by $G_{g_\ell}(\Phi_x, V_g)$, which also depends on the external flux Φ_x. The effective coupling strength between resonators, $\lambda^\pm(\Phi_x) = I_{12}(\Phi_x) \pm G_{12}(\Phi_x)$, comprises both an inductive contribution, $I_{12}(\Phi_x)$, and a capacitive contribution, $G_{12}(\Phi_x)$. It is important to note that all coefficients in the Hamiltonian depend on the external flux Φ_x. We remark that we have used the high-plasma frequency and low-impedance approximation [40, 41], which enables us to express Q_3 and Φ_3 in terms of the other two charge and flux variables.

To analyze the memristive behavior of our device, we consider as input signal the voltage V_g, and the output signal as the signal in the node Φ_2. We study the response of the charge operator in the oscillator 2, considering quantum feedback through the SQUID based on weak measurements on the oscillator 1. We call the initial state of the total system as $|\Psi(0)\rangle$. We update the external magnetic flux after a time Δt according to

$$\frac{\Phi_x^{(j)}}{\Phi_0} = c_1 - c_2\langle\hat{\varphi}_1(t_j)\rangle^2. \tag{6}$$

where c_1 and c_2 are constants and $t_j = j\Delta t$. During the time windows $[t_j, t_{j+1}]$, the magnetic flux is constant and given by $\Phi_x^{(j)}$. To ensure continuous feedback, we use the condition $\omega\Delta t \ll 1$ where ω is the input voltage frequency. This means the time window Δt is much smaller than the input voltage oscillation period, allowing fast updates. Experimentally, we can also replace each LC oscillator with a coplanar waveguide resonator, considering only the fundamental mode, where weak measurements can be performed over microwave photons, and the measurement outcome can be used to provide analog quantum feedback [37–39].

The feedback process modifies the Hamiltonian of the system $\hat{\mathcal{H}}(\Phi_x^{(j)}) \to \hat{\mathcal{H}}(\Phi_x^{(j+1)})$ conditional to the measuring of the expectation value $\langle\hat{\varphi}_1(t_j)\rangle$. In this sense, $\langle\hat{\varphi}_1(t)\rangle$ corresponds to the internal variable $\langle\hat{x}\rangle$ of the memristive system defined in Eq. (3b). The input-output relation of the memristive device is given by the external voltage $V_g(t)$ and $\langle\hat{n}_2(t)\rangle$. In what follows, we will analyze the response of the observable $\langle\hat{n}_2(t)\rangle$ for different initial states and changing the frequency of the external voltage with $V_g(t) = V_0\cos(\omega_\nu t)$.

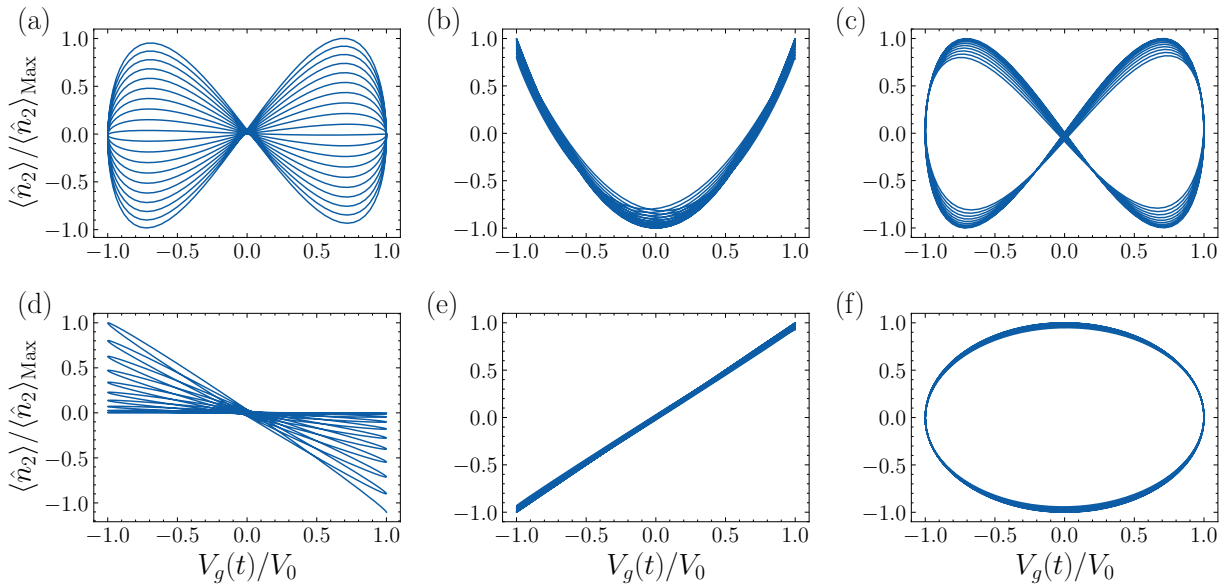

FIG. 2. Dynamic response for different initial states (a) $|\Psi(0)\rangle = |0\rangle \otimes |0\rangle$, $\omega_\nu = \pi/5.92\ \omega_1$ and (b)-(c) $|\Psi(0)\rangle = |0\rangle \otimes |\Psi(\eta,\chi)\rangle$ with $\eta = \pi/2$, for (b) $\chi = 0$, for (c) $\chi = \pi/2$, and $\omega_\nu = \pi/5.94\ \omega_1$. (d)-(f) High-frequency response of the aforementioned cases at $2\omega_\nu$. The calculations used $V_0 = 0.01\mu V$. Coupling strengths $\mathcal{G}_{12}/\omega_1 = 5.294 \times 10^{-3}$, $\mathcal{I}_{12}/\omega_1 = 1.998 \times 10^{-4}$,

IV. SINGLE MICROWAVE QUANTUM MEMRISTOR

In this section, we study the response of the single device to different initial states, and driving frequencies. First, we consider non-correlated initial states. Specifically, we consider the first resonator in the vacuum state and the second in superposition between zero and one photon, coherent and squeezed states, respectively. Afterwards, we consider correlated initial states for both oscillators, such as Bell-like, NOON, and cat states. The values of the constants in Eq. (6) are considered $c_1 = 1.84$ and $c_2 = 0.08$ throughout the analysis. The circuit parameters used in our calculations are summarized in Table I in Appendix A 2.

We study the response of the device modifying the input voltage frequency for two particular values, where we expect to observe pinched hysteresis at a high-frequency regime, where the dynamics tend to behave as a linear resistor. These two behaviors are the fingerprints of a memristive system [6, 27, 42].

A. Non-correlated inputs

We start our analysis considering initial vacuum states for both resonators $|\Psi(0)\rangle = |0\rangle \otimes |0\rangle$. Figure 2(a) shows the evolution of the charge $\langle\hat{n}_2\rangle$ as a function of the external voltage V_g. For the input voltage frequency $\omega_\nu = \pi/5.94\omega_1$, we can see that the curve is pinched at the origin, which can be considered as characteristic of a memristive device [33]. On the other hand, for the input voltage frequency $2\omega_\nu$, high-frequency regime, we observe in Fig. 2(d) that the response tends to a line, which is another feature of memristive behavior. It means our system, starting from the ground state, can be considered a memristive device.

For the case of the initial state $|\Psi(0)\rangle = |0\rangle \otimes |\psi(\eta,\chi)\rangle$, with $|\psi(\eta,\chi)\rangle = \cos(\eta/2)\,|0\rangle + e^{i\chi}\sin(\eta/2)\,|1\rangle$. The dynamical response of the device will be modified as long as we change phase χ. Here, we will consider states with the same amplitudes $\eta = \pi/2$ and choose two values for the relative phase $\chi = \{0, \pi/2\}$. Figure 2(b)-(c) shows the dynamical response of the device for the two mentioned values for the phase χ at driving frequency $\omega_\nu = \pi/5.92\omega_1$. We notice that the value of χ plays the role of control for the memristive feature of our device. For $\chi = 0$, we do not observe a hysteresis loop. However, adjusting $\chi = \pi/2$, it shows a stable hysteresis loop. Moreover, at high-driving frequency, for phase $\chi = 0$, we observe a line, and for $\chi = \pi/2$, we get a circle, which means that the phase χ also modifies the memory effects for the high-frequency regime.

It is interesting to also consider classical initial states, which means coherent states for the second oscillator, $|\Psi(0)\rangle = |0\rangle \otimes |\alpha\rangle$. We characterize the coherent state by its amplitude and phase through the relation $\alpha = re^{i\varphi}$. We consider $r = \pi/4$ and $\varphi = \{\pi/4, \pi/8\}$. Figures 3(a)-(b) show the dynamical response for the two different phases. In both cases, the expectation value of $\langle\hat{n}_2(t)\rangle$ all exhibit the pinched hysteresis curve. Notice that in this case, the phase does not considerably affect the memristive behavior as in the previous case. Also, we observe that for the high-frequency in Fig. 3(e)-(f), we obtain curves with oscillatory features again.

Finally, we can consider another type of classical states like squeezed states defined as $|\Psi(\alpha,\xi)\rangle = \hat{S}(\xi)\,|\alpha\rangle$.Here, $|\alpha\rangle$ is the same coherent state as defined in the previous section, and $\hat{S}(\xi) = \exp(\xi\hat{a}^2 - \xi^*\hat{a}^{\dagger\,2})$ is the squeeze operator. Here, $\xi = Re^{i\theta}$ is also a complex number that characterizes the amount of squeezing and over which resonator quadrature

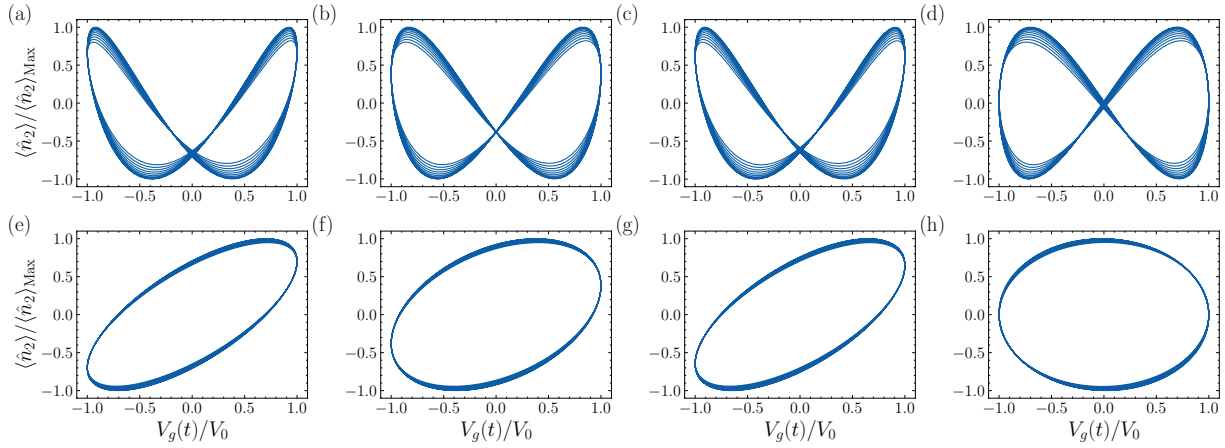

FIG. 3. Dynamic response of the microwave quantum memristor under the action of the input voltage for the initial photonic state $|\Psi(0)\rangle = |0\rangle \otimes |\alpha\rangle \equiv |0\rangle \otimes |re^{i\varphi}\rangle$ with $r = \pi/4$, (a) $\varphi = \pi/4$, whereas (b) $\varphi = \pi/8$. Initial squeezed coherent state $|\Psi(0)\rangle = |0\rangle \otimes |\Psi(\alpha,\xi)\rangle \equiv |0\rangle \otimes \hat{S}(Re^{i\theta})\,|re^{i\varphi}\rangle$, with (c) $R = 0.1$, $\theta = \pi/4$ and (d) $R = 1$, $\theta = \pi/4$. (e)-(h) High-frequency response ($2\omega_\nu$) for the previous states. For both cases, the driving frequencies are identical $\omega_\nu = \pi/5.92\omega_1$. Coupling strength $\mathcal{G}_{12}/\omega_1 = 5.294 \times 10^{-3}$, $\mathcal{I}_{12}/\omega_1 = 2.00 \times 10^{-4}$.

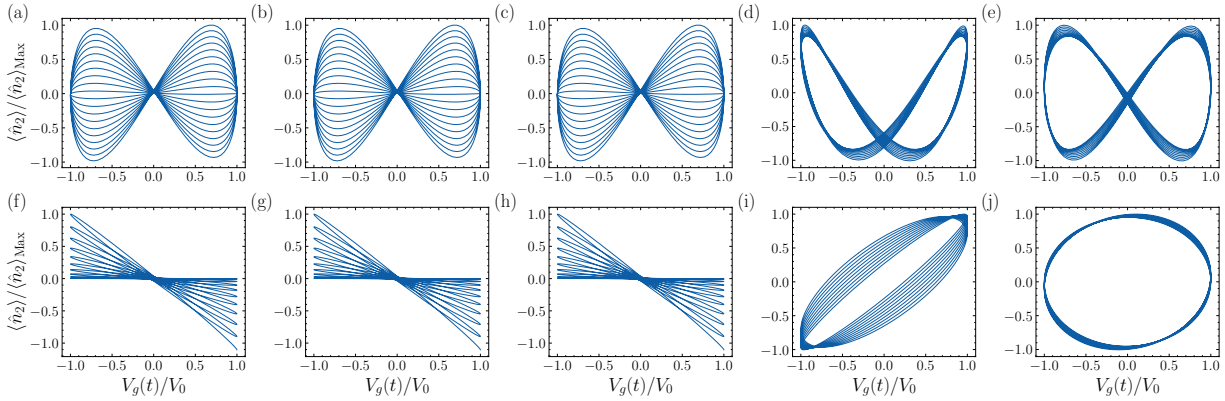

FIG. 4. Dynamic response of the microwave quantum memristor under the action of the input voltage when the system is initialized in the Bell state $|\Psi(0)\rangle = \cos\theta\,|0,0\rangle + \sin\theta\,|1,1\rangle$ where (a) $\theta = \pi/4$, and (b) $\theta = \pi/16$, driving frequency $\omega_\nu = \pi/5.94\omega_1$. (c) Noon state, $|\Psi(0)\rangle = (|2,0\rangle + |0,2\rangle)/\sqrt{2}$. Cat state $|\Psi(0)\rangle = (|\alpha,0\rangle + |0,\alpha\rangle)/\sqrt{2}$ with $\alpha = re^{i\varphi}$, where (d) $r = \pi/2$, $\varphi = \pi/4$ and (e) $r = \pi/2$, $\varphi = \pi/2$ where $\omega_\nu = \pi/5.9\omega_1$. (f)-(j) High-frequency response ($2\omega_\nu$) for the previous states. We consider $V_0 = 0.01\mu V$, whereas the coupling strengths are $\mathcal{G}_{12}/\omega_1 = 5.294 \times 10^{-3}$, $\mathcal{I}_{12}/\omega_1 = 1.998 \times 10^{-4}$.

will be applied. Thus, the initial state of the system is given by $|\Psi(0)\rangle = |0\rangle \otimes |\Psi(\alpha,\xi)\rangle$. In Fig. 3(c)-(d), we observe the input-output dynamics for different squeezing parameters. Specifically we use for Fig. 3(c) and (d) $R = 0.1$ and $R = 1$, respectively, and $\theta = \pi/2$ in both cases. In the high-frequency regime of the input voltage, we see that the system response again looks like an oscillator.

We note that for all classical states (coherent, squeeze, and vacuum) as initial state, our coupled device shows memristive properties in each memristor, making our proposal suitable as a memdevice, at least for classical initialization.

B. Correlated input

An interesting feature of quantum mechanics is the emergence of quantum correlations, which are useful resources to approach quantum advantage in quantum computing. Then, it is important to calculate the dynamical response of our devices for correlated inputs. Specifically, in this section, we consider a Bell-like state, the NOON state, which is a generalization of Bell states for higher photon numbers, and finally, we consider an initial cat state. For the case of Bell-like states, we consider initial superpositions of the form $|\Psi(0)\rangle = \cos(\theta)|0,0\rangle + \sin(\theta)|1,1\rangle$. The dynamics of the system is shown in Fig. 4(a) for $\theta = \pi/4$ and Fig. 4(b) for $\theta = \pi/16$. These two figures show similar results with the vacuum state, which suggests that the memristive properties captured by the hysteresis loop are insensitive to the amount of entanglement. Also, for the high-frequency regime, see Fig. 4(f)-(g), the dynamics tends to a line as the vacuum case, being again insensitive to the initial entanglement in the device. For the case of a NOON state, where we consider $|\Psi(0)\rangle = (|2,0\rangle + |0,2\rangle)/\sqrt{2}$, again the dynamics present

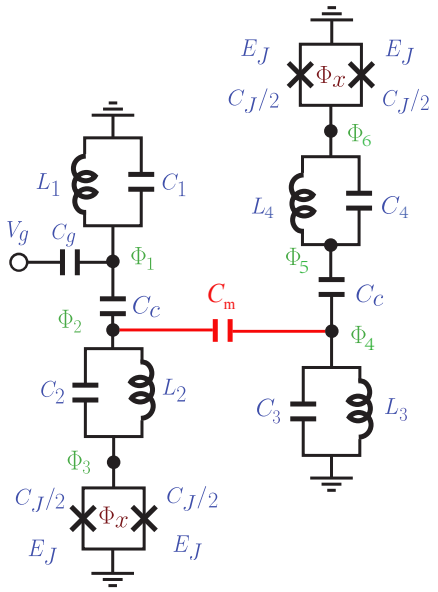

FIG. 5. Coupling of two microwave quantum memristors. The devices are coupled by a capacitor C_m (red color). The second node, Φ_2 in the first device, serves as the input signal to the second device.

the same shape as can be seen in Fig. 4(c) and Fig. 4(h) (high-frequency regime). Finally, for entangled coherent or cat states, we consider $|\Psi(0)\rangle = (|\alpha,0\rangle + |0,\alpha\rangle)/\sqrt{2}$ with $\alpha = re^{i\varphi}$. Here, the dynamics is close to the coherent state case as shown in Fig. 4(d) and (e) for the cases of $\varphi = \pi/4$ and $\varphi = \pi/2$. In both cases with $r = \pi/2$, as well as for the high-frequency regime, that is Figs. 4(i)-(j). These numerical results prove that our proposal keeps the behavior for entangled initial states between both resonators, which means entanglement between the internal variable and the output.

V. COUPLED MICROWAVE QUANTUM MEMRISTORS

We now consider a capacitive coupling between our proposed microwave quantum memristors. Specifically, we consider a coupling between the input node of one device and the output node of the other device as is shown in Fig. 5. We have inverted the second microwave quantum memristor to minimize the crosstalk effect between the SQUIDs. The circuit Hamiltonian for the coupled devices reads (see Appendix B for the complete derivation)

$$\begin{aligned}\hat{\mathcal{H}}_{2M} &= \sum_{\ell=\{1,2\}}\left[\omega_\ell(\Phi_x)\hat{a}_\ell^\dagger\hat{a}_\ell + iG_{g\ell}(\Phi_x,t)(\hat{a}_\ell^\dagger - \hat{a}_\ell) + \Omega_\ell(\Phi_x)\hat{b}_\ell^\dagger\hat{b}_\ell + iJ_{g\ell}(\Phi_x,t)(\hat{b}_\ell^\dagger - \hat{b}_\ell)\right]\\ &+ \lambda^+(\Phi_x)(\hat{a}_1^\dagger\hat{a}_2 + \hat{a}_1\hat{a}_2^\dagger) + \lambda^-(\Phi_x)(\hat{a}_1^\dagger\hat{a}_2^\dagger + \hat{a}_1\hat{a}_2) + \Lambda^+(\Phi_x)(\hat{b}_1^\dagger\hat{b}_2 + \hat{b}_1\hat{b}_2^\dagger) + \Lambda^-(\Phi_x)(\hat{b}_1^\dagger\hat{b}_2^\dagger + \hat{b}_1\hat{b}_2)\\ &+ \sum_{j,k=1}^{2}\left[\gamma_{j,k}^+(\Phi_x)(\hat{a}_j^\dagger\hat{b}_k + \hat{a}_j\hat{b}_k^\dagger) + \gamma_{j,k}^-(\Phi_x)(\hat{a}_j^\dagger\hat{b}_k^\dagger + \hat{a}_j\hat{b}_k)\right]. \end{aligned} \tag{7}$$

Here, $\hat{a}_\ell$ and $\hat{b}_\ell$ stand for the bosonic annihilation operators for each LC oscillator from the ℓth memristive quantum device. Also, $\omega_\ell(\Phi_x)$ and $\Omega_\ell(\Phi_x)$ are the resonator frequency of each microwave quantum memristor, while $G_{g\ell}(\Phi_x)$ and $J_{g\ell}(\Phi_x)$ correspond to the coupling strength between the resonators with the gate voltage. Moreover, $\lambda^\pm(\Phi_x)$ and $\Lambda^\pm(\Phi_x)$ are the coupling strength between the different nodes of each microwave quantum memristor, whereas $\gamma_{j,k}^\pm(\Phi_x)$ is the coupling strength between different devices. We will analyze the coupled case using the same initial state, non-correlated and correlated inputs, for each device of the previous section.

A. Non-correlated inputs for microwave quantum memristors

We analyze the dynamic response of the memristive variable of the coupled device that corresponds to the second oscillator of each subsystem, labeled as oscillator 2 and oscillator 4. We study the evolution of a subsystem during the timescale $T = 10(2\pi)/\omega_\nu$, with ω_ν as the driving frequency of the input voltage. Notice that the coupling capacitance C_m modifies the frequency of both microwave quantum memristor, which leads to a slight change in the conditions required for the input voltage to achieve memristive behavior in both devices. The parameter values used in the analysis are provided in Table II in Appendix B 2.

We start our analysis by considering the initial state $|\Psi(0)\rangle = |0,\psi(\pi/2,0)\rangle\,|0,\psi(\pi/2,0)\rangle$, where $|\psi(\pi/2,0)\rangle = (|0\rangle + |1\rangle)/\sqrt{2}$. We show the response with this initial condition in Fig. 6(a)-(b). We can observe that the observable $\langle\hat{n}\rangle$ exhibits memristive behavior in both microwave quantum memristors. At high frequency, shown in Fig. 6(e)-(f), we can observe that dynamics response form circumference, which corresponds to an oscillatory behavior.

Now, we consider coherent states of the form $|\Psi(0)\rangle = |0,\alpha\rangle\,|0,\alpha\rangle$, where $\alpha = (\pi/2)e^{i\pi/4}$. At voltage frequency $\omega_\nu = 0.5\omega_1$ both devices show pinched hysteresis loop for $\langle\hat{n}\rangle$. Similar to the superposition state, we observe that the memristive response of the second device is more stable than the first one (see Fig. 6(c)-(d)) where again the pinched curve does not shrink or expand. On the other hand, at high frequency ($2\omega_\nu$), the dynamical response of the variable $\langle\hat{n}\rangle$ corresponds again to an oscillator-like behavior.

Finally, we consider as the initial state the state $|\Psi(0)\rangle =$

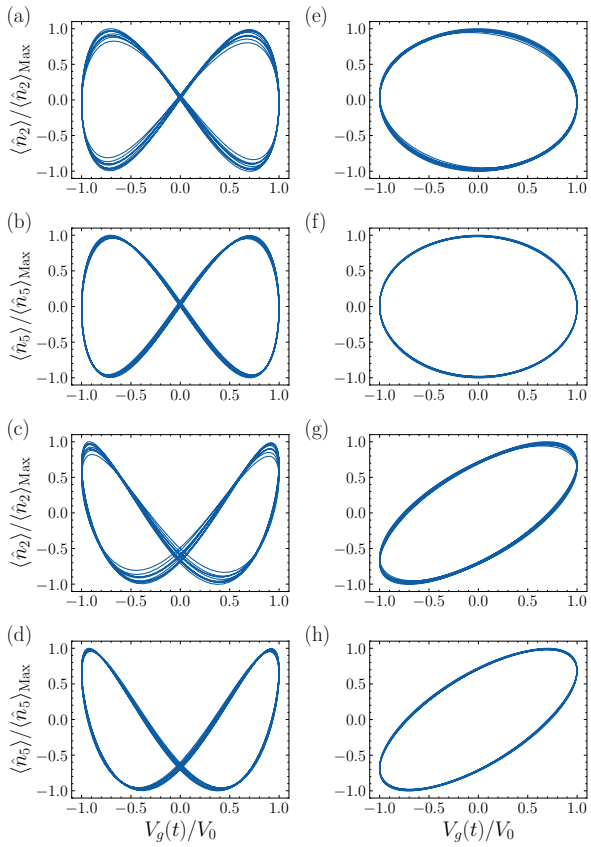

FIG. 6. Dynamic response of the coupled microwave quantum memristors, analyzed using $\hat{n}_2$ and $\hat{n}_5$ under the action of the input voltage when the memristive quantum systems are initialized in (a)-(b) superposition state $|\Psi(0)\rangle = |0,\psi(\eta,\chi)\rangle\,|0,\psi(\eta,\chi)\rangle$, with $\eta = \pi/2$ and $\chi = 0$. (c)-(d) Coherent state $|\Psi(0)\rangle = |0,\alpha\rangle\,|0,\alpha\rangle$, where $\alpha = re^{i\varphi}$ with $r = \pi/2, \varphi = \pi/4$. (a)-(c) $\omega_\nu = \pi/6.33\omega_1$, (b) - (d) $\omega_\nu = \pi/6.25\omega_1$. (e)-(h) High-frequency response ($2\omega_\nu$) for the previous states.

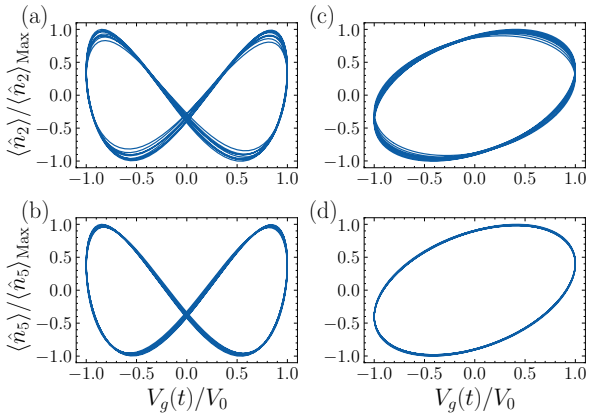

FIG. 7. Dynamic response of coupled microwave quantum memristors utilizing squeezed states in the composite initial state $|\Psi(0)\rangle = |0,\alpha\xi\rangle\,|0,\alpha\xi\rangle$, where $\alpha = re^{i\varphi}$, $\xi = re^{i\varphi}$ ($r = 0.1$, $\varphi = \pi/8$). (a) $\omega_\nu = \pi/6.33\omega_1$, and (b) $\omega_\nu = \pi/6.25\omega_1$. (c) and (d) are the corresponding high-frequency response of the device at double the frequency previously considered.

$|0,\alpha\xi\rangle\,|0,\alpha\xi\rangle$ corresponding to a squeezed state for the resonator 2 and 4, in this case we choose $\alpha = \xi = 0.1e^{\pi/8}$. Similar to the uncoupled case, here we also observe memristive behavior due to the pinched loop at voltage frequency $\omega_{\nu 1} = 0.5\omega_1$ (see Fig. 7). The second memristive system has a more stable response than the first one, maintaining unaltered its pinched hysteresis curve. For the high-frequency response, we see that the system exhibits an elliptical response, looking like an oscillator. This dynamics is similar to the single-device case using the squeezed states.

As a brief conclusion, we can observe that for the case of uncorrelated inputs, the memristive behavior is preserved, obtaining curves with the same shape as in the uncoupled case. Also, we can see that the response of the microwave quantum memristor that is further to the input voltage presents more stable dynamics. This can suggest that for a chain of microwave quantum memristors with uncorrelated inputs, the dynamics will be more stable at the end of the chain.

B. Correlated Input for microwave quantum memristors

As in the case of uncoupled devices, we can calculate the dynamics of coupled devices with initially correlated input states. We use similar states as in the case of a single device it means Bell, NOON, and cat states.

We start our analysis considering Bell state as the initial state, that is $|\Psi(0)\rangle = |\psi_B\rangle\,|\psi_B\rangle$, where $|\psi_B\rangle = (|0,0\rangle + |1,1\rangle)/\sqrt{2}$. Figures 8(a)-(b) show the input-output dynamics for both memristors for $\omega_\nu = 0.5\omega_1$. In this case, curves approach pinched hysteresis loops. We notice that the first device is more stable than the second one. For the high-frequency regime, we can note that the response of the observable $\langle\hat{n}_\ell\rangle$ squashes losing the memristivity (see Fig. 8(e)-(f)).

Next, we initialize the devices a in tensor product of NOON state of the form $|\Psi(0)\rangle = |\psi_N\rangle\,|\psi_N\rangle$, where $|\psi_N\rangle = (|0,2\rangle + |2,0\rangle)/\sqrt{2}$. Interestingly, we observe that for this initialization, the results are similar to Bell states, as depicted in Fig. 8(c)-(d) for voltage frequency $\omega_\nu = 0.5\omega_1$. We need to mention that for Bell and NOON states, the expectation value in the number of photons is zero, which is related to the position of the pinched point in the curves, as pointed out in References [31]. For NOON states, the high-frequency dynamics is similar to the Bell state as can be seen in Fig. 8(g)-(h), where the devices tend to lose their memristive properties.

Finally, we consider an initial cat state $|\Psi(0)\rangle = |\psi_C\rangle\,|\psi_C\rangle$, with $|\psi_C\rangle = (|\alpha,0\rangle + |0,\alpha\rangle)/\sqrt{2}$. For input voltage frequency $\omega_\nu = 0.5\omega_1$ we can obtain pinched hysteresis curves, with a more stable response from the second device, as shown in Fig. 9. On the other hand, at high frequency, the response in the coupled system produces a circle. Therefore, the memristive dynamics is replaced by an oscillatory one.

Again, all these results show that our proposal has memristive quantum properties in each device when coupled in a suitable parameters regime, which can be switched with the frequency of the external input.

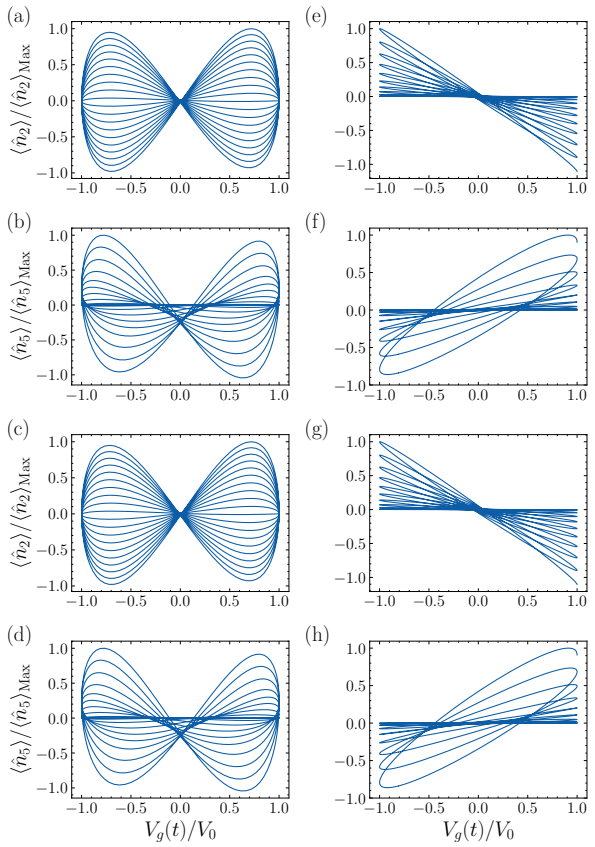

FIG. 8. Dynamic response of the coupled microwave quantum memristors using (a)-(b) Bell state $|\Psi(0)\rangle = |\psi_B\rangle|\psi_B\rangle$, with $|\psi_B\rangle = (|0,0\rangle + |1,1\rangle)/\sqrt{2}$. (c)-(d) NOON state, $|\Psi(0)\rangle = |\psi_N\rangle|\psi_N\rangle$, with $|\psi_N\rangle = (|0,2\rangle + |2,0\rangle)/\sqrt{2}$. The driving frequencies are (a)-(c) $\omega_\nu = \pi/6.3\omega_1$, and (b)-(d) $\omega_\nu = \pi/6.22\omega_1$. (e)-(h) High-frequency response ($2\omega_\nu$) for the previous states.

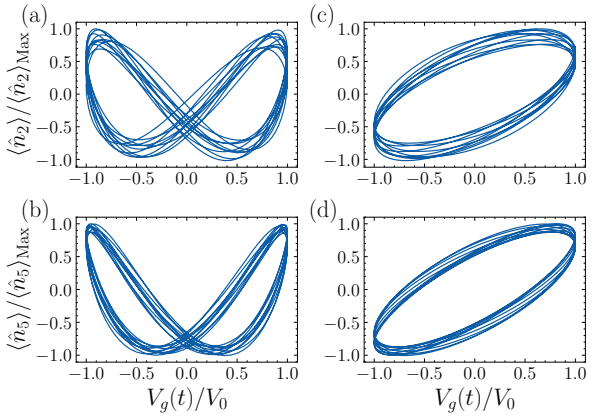

FIG. 9. Dynamic response of second and fourth oscillator using a product of entangled coherent states, $|\Psi(0)\rangle = |\psi_C\rangle|\psi_C\rangle$, where $|\psi_C\rangle = (|\alpha,0\rangle + |0,\alpha\rangle)/\sqrt{2}$ with $\alpha = re^{i\varphi}$ and $r = \pi/2$, $\varphi = \pi/4$. (a) The driving frequency $\omega_\nu = \pi/6.3\omega_1$, and (b) The driving frequency $\omega_\nu = \pi/6.22\omega_1$.

VI. QUANTUM CORRELATIONS

We calculate the correlation embedded in the different resonators of our coupled device described by the reduced density matrix $\rho_{r_i,r_j} = \mathrm{Tr}_{r_k,r_l}(|\Psi\rangle\langle\Psi|)$, where we have traced out two of the resonators. As a measure of quantum correlations, we consider the quantum discord [45, 46], which considers all the correlations in a system that cannot be considered as classical correlations. Formally, quantum discord is defined as

$$\mathcal{Q}_{i,j} = S(\rho_{r_i}) - \min_{\Pi^m_{r_i}} S(\rho_{r_i,r_j|r_j}), \tag{8}$$

where $S(\rho) = \mathrm{Tr}[\rho\log(\rho)]$ is the von Neumann entropy, $\rho_{r_i} = \mathrm{Tr}_{r_j}(\rho_{r_i,r_j})$ and $\rho_{r_i,r_j|r_j}$ is the density matrix after a projective measurement in the resonator r_j. The second term minimizes the von Neumann entropy for all the possible projective measurements in r_j. Such projective measurements can be written as $\Pi^m_{r_j} = \mathbb{I}_{r_i} \otimes U|m\rangle\langle m|U^\dagger$. The d-dimensional unitary matrix U can be written in terms of $d(d-1)/2$ two-level matrices as

$$U = \prod_{k=1}^{d-1}\prod_{n=1}^{d-k} U_{k,n}. \tag{9}$$

Here, the matrix $U_{k,n}$ reads

$$U_{k,n} = \begin{pmatrix} 1 & 0 & .. & & & & & & \\ 0 & 1 & & & & & & & \\ .. & & .. & & & & & & \\ & & & v_{k,k} & & & v_{k,k+n} & & \\ & & & & .. & & & & \\ & & & & & .. & & & \\ & & & v_{k+n,k} & & & v_{k+n,k+n} & & \\ & & & & & & & .. & .. \\ & & & & & & & 1 & 0 \\ & & & & & & & .. & 0 & 1 \end{pmatrix}, \tag{10}$$

where each matrix $U_{k,n}$ can be parametrized in terms of three angles, that is $v_{k,k} = \sin(\phi_1)e^{i\phi_2}$, $v_{k+n,k} = \cos(\phi_1)e^{i\phi_3}$, $v_{k,k+n} = \cos(\phi_1)e^{-i\phi_3}$ and $v_{k+n,k+n} = -\sin(\phi_1)e^{-i\phi_2}$. It means that the U in Eq. (9) can be parametrized by $3(d-1)d/2$ angles, which need to be optimized to minimize the second term in Eq. (8). To perform such an optimization process, we used the basinhopping algorithm from Ref. [47].

Figure 10 shows the dynamics of the quantum correlation for the different resonators in the coupled microwave quantum memristor configuration for different initial states. In Fig. 10 (a)-(c), we consider the bipartite state ρ_{ij} for the ith and jth resonators, we consider initializations in the coherent state, squeezed-displaced state, and superposition state, respectively. As these initial product states possess no inherent correlations, the emergence of finite correlations over time indicates progressive quantum interaction between subsystems. These correlations experience oscillatory behavior, alternating between maximum and minimum values. We note that for the initial superposition state, we reach a non-negligible correlation between the microwave quantum memristors.

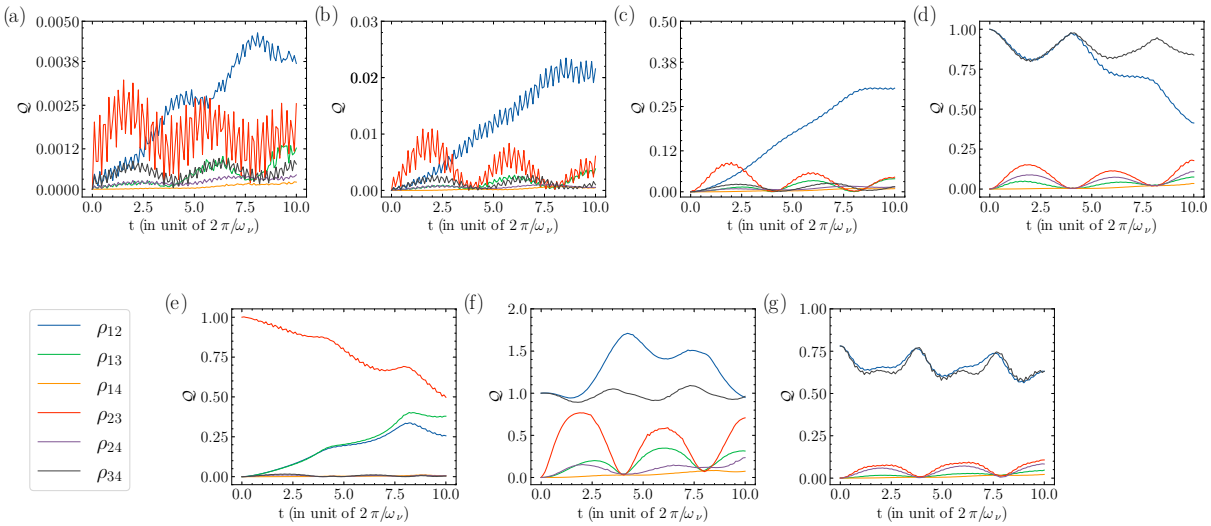

FIG. 10. Quantum discord between different resonators of the coupled QMs in different initial states. ρ_{ij} coresponds to the bipartite state of ith and jth resonator in the device. The initial states are (a) $|\Psi(0)\rangle = |0,\alpha\rangle\,|0,\alpha\rangle$ with $\alpha = \pi/2e^{i\pi/2}$, (b) $|\Psi(0)\rangle = |0,\alpha\xi\rangle\,|0,\alpha\xi\rangle$, where $\alpha = re^{i\varphi}$, $\xi = re^{i\varphi}$ ($r = 0.1$, $\varphi = \pi/8$), (c) $|\Psi(0)\rangle = |0,\psi(\pi/2,0)\rangle\,|0,\psi(\pi/2,0)\rangle$, where $|\psi(\pi/2,0)\rangle\,(|0\rangle + |1\rangle)/\sqrt{2}$, (d) Bell state, $|\Psi(0)\rangle = |\Psi_B\rangle\,|\Psi_B\rangle$, (e) $|\Psi(0)\rangle = |0\rangle\,|\Psi_B\rangle\,|0\rangle$ where $|\psi_B\rangle = \frac{1}{\sqrt{2}}(|00\rangle + |11\rangle)$, (f) Noon state, $|\Psi(0)\rangle = |\psi_N\rangle\,|\psi_N\rangle$, where $|\psi_N\rangle = (|0,2\rangle + |2,0\rangle)/\sqrt{2}$, and (g) Cat coherent state, $|\Psi(0)\rangle = |\psi_C\rangle\,|\psi_C\rangle$, with $|\psi_C\rangle = (|\alpha,0\rangle + |0,\alpha\rangle)/\sqrt{2}$.

Next, we analyze the case when the system starts in an entangled state, Fig. 10(d)-(e), where we consider ρ_{ij} to be in the bell, noon and cast states. In Fig. 10(d), since the system is initialized in a maximally entangled state, ρ_{12} and ρ_{34} start with maximal quantum correlations that decay over time undergoing an oscillatory behavior. It is worth noticing that the oscillations produce a rise and decay in the correlations contained in ρ_{12} and ρ_{34} that coincide with the decay and rise of the correlations contained in ρ_{13}, ρ_{14}, ρ_{23}, ρ_{24}. This implies that the correlations between resonators of the individual microwave quantum memristors get shared over time between the resonators of the different devices. This transfer of quantum correlations is a well-known phenomenon among multipartite systems [48], and their interplay with memristive behavior has been reported recently in SQUID-based quantum memristor [31, 32].

Changing to a different initialization, the 2nd and 3rd resonators can be initialized in a Bell state. The plots corresponding to this configuration are shown in Fig. 10(e). Due to this initial state configuration, the bipartite state ρ_{23} starts from maximal correlations decaying with time and is accompanied by the increase in the correlations of the other bipartite states. We find a similar observation where the maximal (minimal) values of ρ_{23} coincide with the minimal (maximal) values of the other states. Finally, we study the correlations when the system is initialized in the NOON and cat states, as is shown in Fig. 10(f)-(g), where the transfer of correlations is also observed. Using the NOON state, the correlations evolve and go beyond unity since the number of photons in the resonators is 2, and therefore the maximal quantum correlation is not bounded to the unit. Similarly, using the cat state, the correlations depend on the value of α that determines the maximal correlations in the system.

Our proposal can be easily implemented via capacitive coupling as is shown in Fig. 5. This allows the implementation of more complex arrays of memristive quantum devices, opening the door to the experimental implementation of neuromorphic quantum computing and simulation systems.

CONCLUSIONS

We proposed an experimentally feasible quantum memristive device, a microwave quantum memristor, using superconducting circuits in the microwave regime. Our design consists of two coupled resonators grounded through a SQUID, where one of the resonators plays the role of the main system and the other of the auxiliary feedback system. We observe memristive quantum dynamics sd pinched hysteresis curves in the expectation values of the charge variable when we introduce feedback through a magnetic flux in the SQUID. Such magnetic flux depends on weak measurements over the auxiliary resonator. We test these memristive quantum behaviors for different initial states, from classical to entangled inputs.

We showed that our proposal can be easily extended to coupled microwave quantum memristors, allowing for complex networks suitable for developing neuromorphic quantum computers and simulators. In this context, we proved that the memristivity is preserved when we couple two microwave quantum memristors with different classical or quantum initial states. Finally, we displayed that the quantum correlations measured by the quantum discord present nontrivial behaviors, which are fingerprints of the quantumness of our device.

ACKNOWLEDGEMENTS

F.A.-A. acknowledge financial support from Agencia Nacional de Investigación y Desarrollo (ANID): Subvención a la instalación en la Academia No. SA77210018, Fondecyt Regular No, 1231172, and Financiamiento Basal para Centros Científicos y Tecnológicos de Excelencia AFB 220001. F. A. C. L. acknowledge financial support from the German Ministry for Education and Research, under QSolid, Grant No. 13N16149.

Appendix A: Derivation of the circuit Hamiltonian for a single microwave quantum memristor

This section is devoted to deriving the quantized Hamiltonian of the architecture shown in Fig. 1. We derive the classical Hamiltonian and obtain a simplified version of the Hamiltonian using genuine approximations. Finally, we will quantize the Hamiltonian by promoting the charge and flux coordinates to the quantum operators.

1. Classical Hamiltonian for a single microwave quantum memristor

The Lagrangian of the circuit given in Fig. (1) is

$$\mathcal{L} = \frac{C_1}{2}\dot{\Phi}_1^2 - \frac{\Phi_1^2}{2L_1} + \frac{C_g}{2}(\dot{\Phi}_1 - V_g)^2 + \frac{C_c}{2}(\dot{\Phi}_1 - \dot{\Phi}_2)^2 + \frac{C_2}{2}(\dot{\Phi}_2 - \dot{\Phi}_3)^2 - \frac{(\Phi_2 - \Phi_3)^2}{2L_2} + \frac{C_J}{2}\dot{\Phi}_3^2 + 2E_J\cos(\varphi_x)\cos(\varphi_3), \quad \text{(A1)}$$

where $\varphi_3 = 2\pi\Phi_3/\Phi_0$ is the superconducting phase, with $\Phi_0 = h/2e$ as the quantum flux where h is the Planck's constant and $2e$ is the Cooper-pair electric charge. Moreover, $\varphi_x = 2\pi\Phi_x/\Phi_0$ is the external flux through the SQUID. We calculate the canonical conjugate momenta (node charge) through the relation $\mathcal{Q}_n = \partial\mathcal{L}/\partial\dot{\Phi}_n$,

$$\mathcal{Q}_1 = (C_g + C_1 + C_c)\dot{\Phi}_1 - C_c\dot{\Phi}_2 - C_gV_g, \quad \mathcal{Q}_2 = -C_c\dot{\Phi}_1 + C_c\dot{\Phi}_2 + C_2(\dot{\Phi}_2 - \dot{\Phi}_3), \quad \mathcal{Q}_3 = C_2(\dot{\Phi}_3 - \dot{\Phi}_2) + C_J\dot{\Phi}_3. \quad \text{(A2)}$$

By defining $\tilde{\mathcal{Q}}_1 = \mathcal{Q}_1 + C_gV_g$, $\tilde{\mathcal{Q}}_2 = \mathcal{Q}_2$, $\tilde{\mathcal{Q}}_3 = \mathcal{Q}_3$, the set of equations given in Eq. (A2) can be written as $\vec{\tilde{\mathcal{Q}}} = \hat{C}\dot{\vec{\Phi}}$. Here, $\vec{\tilde{\mathcal{Q}}}$ and $\dot{\vec{\Phi}}$ correspond to the charge and time derivative flux vector, respectively, and $\hat{C}$ is the capacitance matrix. Applying the Legendre transformation $\mathcal{H} = \sum_i \tilde{\mathcal{Q}}_i\dot{\Phi}_i - \mathcal{L}$, we obtain the circuit Hamiltonian as

$$\mathcal{H} = \frac{C_{11}^{-1}\tilde{\mathcal{Q}}_1^2}{2} + \frac{C_{22}^{-1}\tilde{\mathcal{Q}}_2^2}{2} + \frac{C_{33}^{-1}\tilde{\mathcal{Q}}_3^2}{2} + C_{12}^{-1}\tilde{\mathcal{Q}}_1\tilde{\mathcal{Q}}_2 + C_{13}^{-1}\tilde{\mathcal{Q}}_1\tilde{\mathcal{Q}}_3 + C_{23}^{-1}\tilde{\mathcal{Q}}_2\tilde{\mathcal{Q}}_3 + \frac{\Phi_1^2}{2L_1} + \frac{(\Phi_2 - \Phi_3)^2}{2L_2} - 2E_J\cos(\varphi_x)\cos(\varphi_3). \quad \text{(A3)}$$

Here, C_{ij}^{-1} corresponds to the matrix elements of the inverse of the capacitance matrix given by

$$\hat{C}^{-1} = \frac{1}{C^\star}\begin{pmatrix} C_cC_J + C_2(C_c + C_J) & C_c(C_J + C_2) & C_2C_c \\ C_c(C_J + C_2) & (C_c + C_1 + C_g)(C_J + C_2) & C_2(C_c + C_1 + C_g) \\ C_2C_c & C_2(C_c + C_1 + C_g) & C_cC_g + C_2(C_c + C_g) + C_1(C_c + C_2) \end{pmatrix},$$

where $C^\star = C_2C_c(C_1 + C_g) + C_J(C_1(C_2 + C_c) + C_cC_g + C_2(C_c + C_g))$. Notice that the system dynamics of our circuit depends on three degrees of freedom $\{\Phi_1, \Phi_2, \Phi_3\}$ corresponding to the two resonators and the SQUID, respectively. We may reduce the system dynamics in terms of $\{\Phi_1, \Phi_2\}$ considering the high-plasma frequency ($\dot{\Phi}_3 \ll \dot{\Phi}_{1(2)}$ ($\ddot{\Phi}_3 \ll \ddot{\Phi}_{1(2)}$) and low-impedance regime ($\Phi_3 \ll \Phi_{1(2)}$) of the SQUID [49], obtaining the relation between the node charges as

$$\tilde{\mathcal{Q}}_3 = \left(\frac{-C_2C_c}{C_2(C_1 + C_g) + C_c(C_1 + C_g + C_2)}\tilde{\mathcal{Q}}_1 + \frac{-C_2(C_c + C_1 + C_g)}{C_2(C_1 + C_g) + C_c(C_1 + C_g + C_2)}\tilde{\mathcal{Q}}_2\right). \quad \text{(A4)}$$

Next, we derive the relation between the node fluxes using the Euler-Lagrange equation $\partial\mathcal{L}/\partial\Phi_i - d(\partial\mathcal{L}/\partial\dot{\Phi}_i)/dt = 0$ and considering high-plasma frequency $\ddot{\Phi}_3 \ll \ddot{\Phi}_{1(2)}$

$$-\frac{\Phi_1}{L_1} + C_c\ddot{\Phi}_2 - (C_c + C_1 + C_g)\ddot{\Phi}_1 = 0, \quad -\frac{\Phi_2}{L_2} - (C_c + C_2)\ddot{\Phi}_2 + C_c\ddot{\Phi}_1 = 0, \quad \frac{4\pi E_J\cos(\varphi_x)}{\Phi_0}\sin(\varphi_3) + C_2\ddot{\Phi}_2 = 0. \tag{A5}$$

We get Φ_3 from Φ_1 and Φ_2 using the second linearized regime of the Josephson junction [50] i.e., $\sin(\varphi_3) = \varphi_3$ leading to

$$\varphi_3 = \frac{\Phi_0}{4\pi E_J\cos(\varphi_x)}\left(\alpha_1\frac{\Phi_1}{L_1} + \alpha_2\frac{\Phi_2}{L_2}\right), \tag{A6}$$

where $\alpha_1 = \frac{C_2C_c}{(C_c+C_1+C_g)(C_c+C_2)-C_c^2}$ and $\alpha_2 = \frac{C_2(C_c+C_1+C_g)}{(C_c+C_1+C_g)(C_c+C_2)-C_c^2}$. We note that

$$\alpha_2 = \alpha_1 + \frac{C_2(C_1+C_g)}{(C_c+C_1+C_g)(C_c+C_2)-C_c^2}. \tag{A7}$$

To express the Hamiltonian in terms of Eq. (A6), we consider the low-impedance regime ($\Phi_3 \ll \Phi_{1(2)}$), so that $\cos(\varphi_3) = 1-\varphi_3^2/2$ and keep the potential energy of the SQUID up to the second order. Using Eq. (A4) and Eq. (A6) in Eq. (A3) we arrive at the Hamiltonian given by

$$\mathcal{H} = \frac{\mathcal{Q}_1^2}{2\tilde{C}_1} + \frac{\mathcal{Q}_2^2}{2\tilde{C}_2} + \frac{\Phi_1^2}{2\tilde{L}_1(\Phi_x)} + \frac{\Phi_2^2}{2\tilde{L}_2(\Phi_x)} + \frac{\mathcal{Q}_1\mathcal{Q}_2}{\tilde{C}_{12}} + \frac{\mathcal{Q}_1\mathcal{Q}_g}{\tilde{C}_{1g}} + \frac{\mathcal{Q}_2\mathcal{Q}_g}{\tilde{C}_{2g}} + \frac{\Phi_1\Phi_2}{\tilde{L}_{12}(\Phi_x)}, \tag{A8}$$

where we have used $\tilde{\mathcal{Q}}_1 = \mathcal{Q}_1 + C_gV_g$, $\tilde{\mathcal{Q}}_2 = \mathcal{Q}_2$ and defined the following dressed circuit parameters

$$\begin{aligned}
&\tilde{C}_1 = \tilde{C}_{1g} = \frac{(C_2+C_g)(C_1+C_g)+C_cC_2}{C_2+C_c}, \tilde{C}_2 = \frac{(C_2+C_g)(C_1+C_g)+C_cC_2}{C_c+C_1+C_g}, \tilde{L}_i(\Phi_x) = \frac{L_i^2}{L_i + \frac{\Phi_0^2\alpha_i^2}{8\pi^2E_J\cos(\varphi_x)}}, \\
&\tilde{C}_{12} = \tilde{C}_{2g} = \frac{(C_2+C_g)(C_1+C_g)+C_cC_2}{C_c}, \tilde{L}_{12}(\Phi_x) = \frac{4\pi^2E_J\cos(\varphi_x)L_1L_2}{\alpha_1\alpha_2\Phi_0^2}.
\end{aligned} \tag{A9}$$

2. Quantization of the Hamiltonian for a single microwave quantum memristor

To proceed with the quantum mechanical description of the system, we promote the classical variables to quantum operators using $\hat{Q}_\ell = 2e\hat{n}_\ell$, $\hat{\Phi}_\ell = (\hat{\varphi}_\ell/2\pi)\Phi_0$, where $\hat{n}_\ell$ and $\hat{\varphi}_\ell$ are the cooper pair charge and phase operators, respectively, satisfying $[\hat{\Phi}_\ell, \hat{Q}_{\ell'}] = i\hbar\delta_{\ell,\ell'}$. Then, the Hamiltonian in Eq. (A8) can be written as

$$\hat{\mathcal{H}} = \sum_{\ell=1,2}\left[4E_{C\ell}\hat{n}_\ell^2 + \frac{E_{L\ell}(\Phi_x)}{2}\hat{\varphi}_\ell^2 + 8E_{C\ell g}\hat{n}_\ell n_g\right] + 8E_{C12}\hat{n}_1\hat{n}_2 + E_{L12}(\Phi_x)\hat{\varphi}_1\hat{\varphi}_2, \tag{A10}$$

where $n_g = \mathcal{Q}_g/2e$ is the dimensionless gate charge, $E_{C\ell} = e^2/2\tilde{C}_\ell$ and $E_{L\ell}(\Phi_x) = \Phi_0^2/(4\pi^2\tilde{L}_\ell(\Phi_x))$ are the charge and inductive energies, respectively, while $E_{C12} = e^2/2\tilde{C}_{12}$ and $E_{L12}(\Phi_x) = \Phi_0^2/(4\pi^2\tilde{L}_{12}(\Phi_x))$ are the coupling energies. Finally, we define the coupling energy of the lth resonator with the gate voltage as $E_{C\ell g} = e^2/2\tilde{C}_{\ell g}$. The charge and phase operators can be written in terms of the annihilation and creation operators, $\hat{n}_\ell = in_\ell(\hat{a}_\ell^\dagger - \hat{a}_\ell)$ and $\hat{\varphi}_\ell = \varphi_\ell(\hat{a}_\ell^\dagger + \hat{a}_\ell)$, where $n_\ell = (E_{L\ell}/32E_{C\ell})^{1/4}$, $\varphi_\ell = (2E_{C\ell}/E_{L\ell})^{1/4}$ correspond to zero point fluctuations, leading to the following quantum Hamiltonian

$$\hat{\mathcal{H}} = \sum_{\ell=1,2}\left[\hbar\omega_\ell(\Phi_x)\hat{a}_\ell^\dagger\hat{a}_\ell + iG_{g\ell}(\Phi_x,t)(\hat{a}_\ell^\dagger - \hat{a}_\ell)\right] + \lambda^-(\Phi_x)(\hat{a}_1^\dagger\hat{a}_2^\dagger + \hat{a}_1\hat{a}_2) + \lambda^+(\Phi_x)(\hat{a}_1^\dagger\hat{a}_2 + \hat{a}_1\hat{a}_2^\dagger), \tag{A11}$$

where $\omega_\ell(\Phi_x) = \sqrt{8E_{C\ell}E_{L\ell}(\Phi_x)}/\hbar$ is the frequency of the ℓth resonator. Also, $G_{g\ell}(\Phi_x,t)$ corresponds to the coupling strength with the external time-dependent gate voltage. Moreover, $\lambda^\pm(\Phi_x) = I_{12}(\Phi_x) \pm G_{12}(\Phi_x)$ is the effective coupling strength where

$I_{12}(\Phi_x)$ and $G_{12}(\Phi_x)$ are the tunable inductive and capacitive coupling strengths, respectively. They are expressed as

$$\begin{aligned} G_{g\ell}(\Phi_x,t) &= 8E_{C\ell g}n_g\left(\frac{E_{L\ell}(\Phi_x)}{32E_{C\ell}}\right)^{1/4}, \\ G_{12}(\Phi_x) &= 2E_{C12}\left(\frac{E_{L1}(\Phi_x)E_{L2}(\Phi_x)}{4E_{C1}E_{C2}}\right)^{1/4}, \\ I_{12}(\Phi_x) &= E_{L12}\left(\frac{4E_{C1}E_{C2}}{E_{L1}(\Phi_x)E_{L2}(\Phi_x)}\right)^{1/4}. \end{aligned}$$

The circuit and system parameters obtained after constrained optimization based on the mentioned approximations are summarized in the following Table I,

TABLE I. Optimal circuit parameters.

Circuit Parameters							
C_c [fF]	C_1 [fF]	C_2[fF]	C_J [fF]	C_g [fF]	L_1 [pH]	L_2 [pH]	$E_J/2\pi$ [GHz]
5.657	413.5	530.4	536	116.9	746.2	749.8	219.1
System parameters							
ω_1 [GHz]	ω_2 [GHz]	ω_S [GHz]	G_{12}/ω_1	I_{12}/ω_1	Z_1/Z_S	Z_2/Z_S	ω_S/ω_1
5	5	50	0.005	0.00005	9.999	9.999	10

Appendix B: Derivation of the circuit Hamiltonian for coupled microwave quantum memristors

In this section, we derive the quantum Hamiltonian of the coupled microwave quantum memristors of Fig. (5).

1. Classical Hamiltonian for coupled microwave quantum memristors

The coupled system is described by the Lagrangian

$$\begin{aligned} \mathcal{L} =& \frac{C_1}{2}\dot{\Phi}_1^2 + \frac{C_3}{2}\dot{\Phi}_4^2 - \frac{\Phi_1^2}{2L_1} - \frac{\Phi_4^2}{2L_3} + \frac{C_c}{2}\big\{(\dot{\Phi}_1-\dot{\Phi}_2)^2 + (\dot{\Phi}_2-\dot{\Phi}_3)^2\big\} + \frac{C_2}{2}(\dot{\Phi}_2-\dot{\Phi}_3)^2 + \frac{C_4}{2}(\dot{\Phi}_5-\dot{\Phi}_6)^2 - \frac{(\Phi_2-\Phi_3)^2}{2L_2} \\ & - \frac{(\Phi_5-\Phi_6)^2}{2L_4} + \frac{C_J}{2}(\dot{\Phi}_3^2+\dot{\Phi}_6^2) + 2E_J\cos(\varphi_x)\big\{\cos(\varphi_3)+\cos(\varphi_6)\big\} + \frac{C_m}{2}(\dot{\Phi}_2-\dot{\Phi}_4)^2 + \frac{C_g}{2}(\dot{\Phi}_1-V_g)^2, \end{aligned} \tag{B1}$$

where $\varphi_3 = 2\pi\Phi_3/\Phi_0$ and $\varphi_6 = 2\pi\Phi_6/\Phi_0$ are the superconducting phases in the respective devices, while $\varphi_x = 2\pi\Phi_x/\Phi_0$ is the external flux through the SQUID. Using the relation $\mathcal{Q}_n = \partial\mathcal{L}/\partial\dot{\Phi}_n$, we obtain the relation between the node charges as

$$\begin{aligned} &\mathcal{Q}_1 = (C_g+C_1+C_c)\dot{\Phi}_1 - C_c\dot{\Phi}_2 - C_gV_g, \quad \mathcal{Q}_2 = -C_c\dot{\Phi}_1 + (C_c+C_m+C_2)\dot{\Phi}_2 - C_2\dot{\Phi}_3 - C_m\dot{\Phi}_4, \\ &\mathcal{Q}_3 = -C_2\dot{\Phi}_2 + (C_J+C_2)\dot{\Phi}_3, \quad \mathcal{Q}_4 = -C_m\dot{\Phi}_2 - (C_c+C_m+C_3)\dot{\Phi}_4 - C_c\dot{\Phi}_5, \\ &\mathcal{Q}_5 = -C_c\dot{\Phi}_4 - (C_c+C_4)\dot{\Phi}_5 - C_4\dot{\Phi}_6, \quad \mathcal{Q}_6 = -C_4\dot{\Phi}_5 + (C_J+C_4)\dot{\Phi}_6. \end{aligned} \tag{B2}$$

Similar to the previous section, we define $\tilde{\mathcal{Q}}_1 = \mathcal{Q}_1 + C_gV_g$, $\tilde{\mathcal{Q}}_2 = \mathcal{Q}_2$, $\tilde{\mathcal{Q}}_3 = \mathcal{Q}_3$, $\tilde{\mathcal{Q}}_4 = \mathcal{Q}_4$, $\tilde{\mathcal{Q}}_5 = \mathcal{Q}_5$, and $\tilde{\mathcal{Q}}_6 = \mathcal{Q}_6$. The set of relations given in Eq. (B2) can be written as $\vec{\tilde{\mathcal{Q}}} = \hat{C}\dot{\vec{\Phi}}$. By using the Legendre transformation $\mathcal{H} = \sum_n \mathcal{Q}_n\dot{\Phi}_n - \mathcal{L}$, we get the circuit Hamiltonian

$$\begin{aligned} \mathcal{H}_{2M} = & \sum_{i,j=1(i\neq j)}^{6} \frac{1}{2}\big(\tilde{Q}_i^2C_{i,i}^{-1} + \tilde{Q}_i\tilde{Q}_jC_{i,j}^{-1}\big) + \frac{\Phi_1^2}{2L_1} + \frac{(\Phi_2-\Phi_3)^2}{2L_2} + \frac{\Phi_4^2}{2L_3} + \frac{(\Phi_5-\Phi_6)^2}{2L_4} \\ & - 2E_J\cos(\varphi_x)\big\{\cos(\varphi_3)+\cos(\varphi_6)\big\}, \end{aligned} \tag{B3}$$

where C_{ij}^{-1} corresponds to the inverse capacitance matrix element of $\hat{C}$. As with a single microwave quantum memristor, we consider the low-impedance regime of the SQUIDs ($\dot{\Phi}_3 \ll \dot{\Phi}_{1(2)}, \dot{\Phi}_6 \ll \dot{\Phi}_{4(5)}$) obtaining the relation between the node charges

$$\tilde{\mathcal{Q}}_3 = -C_2(B_{21}^{-1}\tilde{\mathcal{Q}}_1 + B_{22}^{-1}\tilde{\mathcal{Q}}_2 + B_{23}^{-1}\tilde{\mathcal{Q}}_4 + B_{24}^{-1}\tilde{\mathcal{Q}}_5), \quad \tilde{\mathcal{Q}}_6 = -C_4(B_{41}^{-1}\tilde{\mathcal{Q}}_1 + B_{42}^{-1}\tilde{\mathcal{Q}}_2 + B_{43}^{-1}\tilde{\mathcal{Q}}_4 + B_{44}^{-1}\tilde{\mathcal{Q}}_5), \tag{B4}$$

where B_{ij}^{-1} are the elements of the inverse of matrix $\hat{B}$ given by

$$\hat{B} = \begin{pmatrix} C_c + C_g + C_1 & -C_c & 0 & 0 \\ -C_c & C_c + C_m + C_2 & -C_m & 0 \\ 0 & -C_m & C_c + C_m + C_3 & -C_c \\ 0 & 0 & -C_c & C_c + C_4 \end{pmatrix}. \tag{B5}$$

Similarly, for the node fluxes, using the Euler-Lagrange equation $\partial\mathcal{L}/\partial\Phi_i - d(\partial\mathcal{L}/\partial\dot{\Phi}_i)/dt = 0$ and considering second linearized regime of the Junctions ($\sin(\varphi_{3(6)}) = \varphi_{3(6)}$) and low-impedance regime of the SQUIDs ($\ddot{\Phi}_3 \ll \ddot{\Phi}_{1(2)}$, $\ddot{\Phi}_6 \ll \ddot{\Phi}_{4(5)}$), we get

$$\varphi_{3(6)} = \frac{(-C_{2(4)})\Phi_0}{4\pi E_J \cos(\varphi_x)} \left(B_{2(4)1}^{-1} \frac{\Phi_1}{L_1} + B_{2(4)2}^{-1} \frac{\Phi_2}{L_2} + B_{2(4)3}^{-1} \frac{\Phi_4}{L_3} + B_{2(4)4}^{-1} \frac{\Phi_5}{L_4} \right). \tag{B6}$$

Furthermore, we express the Hamiltonian in terms of Eq. (B6) considering high plasma frequency($\Phi_3 \ll \Phi_{1(2)}$, $\Phi_6 \ll \Phi_{4(5)}$) and approximating $\cos(\varphi_{3(6)}) \approx 1 - \varphi_{3(6)}^2$. Using Eq. (B4) and Eq. (B6) in Eq. (B3), we obtain

$$\mathcal{H}_{2M} = \sum_{i=1}^{2} \mathcal{H}_i + \mathcal{H}_c, \tag{B7}$$

where $\mathcal{H}_i$ is the Hamiltonian of the single microwave quantum memristor derived in the last section, Eq. (A8), and the coupling Hamiltonian is

$$\mathcal{H}_c = \frac{\mathcal{Q}_1\mathcal{Q}_4}{\tilde{C}_{13}} + \frac{\mathcal{Q}_1\mathcal{Q}_5}{\tilde{C}_{14}} + \frac{\mathcal{Q}_2\mathcal{Q}_4}{\tilde{C}_{23}} + \frac{\mathcal{Q}_2\mathcal{Q}_5}{\tilde{C}_{24}} + \frac{\Phi_1\Phi_4}{\tilde{L}_{13}} + \frac{\Phi_1\Phi_5}{\tilde{L}_{14}} + \frac{\Phi_2\Phi_4}{\tilde{L}_{23}} + \frac{\Phi_2\Phi_5}{\tilde{L}_{24}}.$$

Here, we have used $\tilde{\mathcal{Q}}_1 = \mathcal{Q}_1 + C_g V_g$, $\tilde{\mathcal{Q}}_2 = \mathcal{Q}_2$, $\tilde{\mathcal{Q}}_3 = \mathcal{Q}_3$, the effective coupling capacitances are defined as

$$\begin{aligned} \tilde{C}_{m,n(m=1,2;n=3,4)} = \Big(& C_{m,n+1}^{-1} + C_{3,3}^{-1} C_2^2 B_{2,m}^{-1} b_{2,n}^{-1} - C_2 C_{m,3}^{-1} B_{2n}^{-1} - C_2 C_{3,n+1}^{-1} B_{2,m}^{-1} + C_4^2 C_{6,6}^{-1} B_{4,m}^{-1} B_{4,n}^{-1} - C_4 C_{m,6}^{-1} B_{4,n}^{-1} \\ & - C_4 C_{n+1,6} B_{4,m}^{-1} + C_4 C_2 C_{3,6}^{-1} B_{2,m}^{-1} B_{4,n}^{-1} + C_4 C_2 C_{3,6}^{-1} B_{2,n}^{-1} B_{4,m}^{-1} \Big)^{-1}, \end{aligned}$$

and the effective coupling inductances reads

$$\tilde{L}_{m,n(m=1,2,n=3,4)} = \frac{4\pi E_J \cos(\varphi_x)}{\Phi_0^2} \left(\frac{{C_2}^2 B_{2,m}^{-1} B_{2,n}^{-1}}{L_m L_n} + \frac{{C_4}^2 B_{4,m}^{-1} B_{4,n}^{-1}}{L_m L_n} \right)^{-1}.$$

2. Quantization of the Hamiltonian for coupled microwave quantum memristors

By promoting the charge and phase variables to quantum operators, using $\hat{Q}_\ell = 2e\hat{n}_\ell$, $\hat{\Phi}_\ell = (\hat{\varphi}_\ell/2\pi)\Phi_0$ to satisfy the canonical commutation relation $[\,\hat{\Phi}_\ell, \hat{Q}_{\ell'}] = i\hbar\delta_{\ell,\ell'}$, we obtain the quantum Hamiltonian of the coupled microwave quantum memristors as

$$\hat{\mathcal{H}}_{2M} = \sum_{i=1}^{2} \hat{\mathcal{H}}_i + \hat{\mathcal{H}}_c. \tag{B8}$$

Here, $\hat{\mathcal{H}}_i$ is the quantum Hamiltonian of a single microwave quantum memristor (see Eq. (A10)) and the quantized coupling Hamiltonian $\hat{\mathcal{H}}_c$ reads

$$\hat{\mathcal{H}}_c = \textstyle\sum_{n=1(2),m=3(4)} \left(4E_{Cnm}\hat{n}_n\hat{n}_{m+1} + E_{Lnm}\hat{\varphi}_n\hat{\varphi}_{m+1} \right), \tag{B9}$$

where the coupling capacitance and inductance energies are $E_{Cnm(n=1,2,m=3,4)} = e^2/(2\tilde{C}_{nm})$, $E_{Lnm(n=1,2,m=3,4)}(\Phi_x) = \Phi_0^2/(4\pi^2\tilde{L}_{nm}(\Phi_x))$. We express the charge and phase operators in terms of the annihilation and creation operators

$$\begin{aligned} \hat{n}_{1(2)} &= in_{1(2)}(\hat{a}_{1(2)}^\dagger - \hat{a}_{1(2)}), \quad \hat{\varphi}_{1(2)} = \varphi_{1(2)}(\hat{a}_{1(2)}^\dagger + \hat{a}_{1(2)}), \\ \hat{n}_{4(5)} &= in_{4(5)}(\hat{b}_{1(2)}^\dagger - \hat{b}_{1(2)}), \quad \hat{\varphi}_{4(5)} = \varphi_{4(5)}(\hat{b}_{1(2)}^\dagger + \hat{b}_{1(2)}), \end{aligned}$$

where $n_{1(2)} = (E_{L1(2)}/32E_{C1(2)})^{1/4}$, $\varphi_{1(2)} = (2E_{C1(2)}/E_{L1(2)})^{1/4}$, $n_{4(5)} = (E_{L3(4)}/32E_{C3(4)})^{1/4}$, $\varphi_{4(5)} = (2E_{C3(4)}/E_{L3(4)})^{1/4}$ with $E_{C\ell=1,2,3,4} = e^2/2\tilde{C}_\ell$, $E_{L\ell=1,2,3,4}(\Phi_x) = \Phi_0^2/(4\pi^2\tilde{L}_\ell(\Phi_x))$. Then, we obtain the second quantized Hamiltonian

$$\hat{\mathcal{H}}_1 = \sum_{\ell=1,2}\left[\omega_\ell(\Phi_x)\hat{a}_\ell^\dagger\hat{a}_\ell + iG_{g\ell}(\Phi_x,t)(\hat{a}_\ell^\dagger - \hat{a}_\ell)\right] + \lambda^+(\Phi_x)(\hat{a}_1^\dagger\hat{a}_2 + \hat{a}_1\hat{a}_2^\dagger) + \lambda^-(\Phi_x)(\hat{a}_1^\dagger\hat{a}_2^\dagger + \hat{a}_1\hat{a}_2),$$

$$\hat{\mathcal{H}}_2 = \sum_{\ell=1,2}\left[\Omega_\ell(\Phi_x)\hat{b}_\ell^\dagger\hat{b}_\ell + iJ_{g\ell}(\Phi_x,t)(\hat{b}_\ell^\dagger - \hat{b}_\ell)\right] + \Lambda^+(\Phi_x)(\hat{b}_1^\dagger\hat{b}_2 + \hat{b}_1\hat{b}_2^\dagger) + \Lambda^-(\Phi_x)(\hat{b}_1^\dagger\hat{b}_2^\dagger + \hat{b}_1\hat{b}_2),$$

$$\hat{\mathcal{H}}_c = \sum_{j,k=1}^{2}\left[\gamma_{j,k}^+(\Phi_x)(\hat{a}_j^\dagger\hat{b}_k + \hat{a}_j\hat{b}_k^\dagger) + \gamma_{j,k}^-(\Phi_x)(\hat{a}_j^\dagger\hat{b}_k^\dagger + \hat{a}_j\hat{b}_k)\right],$$

where $\omega_{1(2)}(\Phi_x) = \sqrt{8E_{C1(2)}E_{L1(2)}(\Phi_x)}/\hbar$ and $\Omega_{1(2)}(\Phi_x) = \sqrt{8E_{C3(4)}E_{L3(4)}(\Phi_x)}/\hbar$ are the frequencies of the resonator in each microwave quantum memristor. Also, $G_{g\ell}(\Phi_x,t)$ and $J_{g\ell}(\Phi_x,t)$ corresponds to the coupling strength between the resonators with gate voltage. Here, $\lambda^\pm(\Phi_x) = I_{12}(\Phi_x) \pm G_{12}(\Phi_x)$, and $\Lambda^\pm(\Phi_x) = F_{12}(\Phi_x) \pm J_{12}(\Phi_x)$ are the effective coupling strengths of each single microwave quantum memristor, while $\gamma^\pm(\Phi_x) = K_{j,k}(\Phi_x) \pm M_{j,k}(\Phi_x)$ are the effective coupling strength between oscillators of the two microwave quantum memristors defined as

$$K_{j=1,2,k=3,4}(\Phi_x) = E_{Ljk}(\Phi_x)\left(\frac{4E_{Cj}E_{Ck}}{E_{Lj}(\Phi_x)E_{Lk}(\Phi_x)}\right)^{1/4}, \qquad M_{j=1,2,k=3,4}(\Phi_x) = 2E_{Cjk}\left(\frac{E_{Lj}(\Phi_x)E_{Lk}(\Phi_x)}{4E_{Cj}E_{Ck}}\right)^{1/4}.$$

Finally, we summarize the coupled systeme parameters used in the main text, where Table II shows the optimal case.

TABLE II. Coupled device circuit parameters.

Circuit Parameters							
C_c [fF]	C_1 [fF]	C_2[fF]	C_3 [fF]	C_4[fF]	C_J [fF]	C_g [fF]	C_m[fF]
5.657	413.5	530.4	413.5	530.4	536.0	116.9	11.69
L_1 [pH]	L_2 [pH]	L_3 [pH]	L_4 [pH]	$E_J/2\pi$ [GHz]			
746.2	749.8	746.2	749.8	219.1			
System parameters							
ω_1 [GHz]	ω_2 [GHz]	Ω_1 [GHz]	Ω_2 [GHz]	λ^+/ω_1	λ^-/ω_1	Λ^+/ω_1	Λ^-/ω_1
5	4.97	5.579	5.034	0.00569	-0.00529	0.00652	-0.00597
$\gamma_{1,1}^+\omega_1$	$\gamma_{1,1}^-/\omega_1$	$\gamma_{1,2}^+/\omega_1$	$\gamma_{1,2}^-/\omega_1$	$\gamma_{2,1}^+/\omega_1$	$\gamma_{2,1}^-/\omega_1$	$\gamma_{2,2}^+/\omega_1$	$\gamma_{2,2}^-/\omega_1$
0.000145	-0.000134	0.0	0.0	0.0139	-0.0128	0.00016	-0.00014

[1] D. Marković, A. Mizrahi, D. Querlioz, and J. Grollier, *Physics for neuromorphic computing*, Nat. Rev. Phys. **2**, 499 (2020).

[2] N. K. Upadhyay, H. Jiang, Z. Wang, S. Asapu, Q. Xia, J. J. Yang, *Emerging Memory Devices for Neuromorphic Computing*, Adv. Mater. Technol. **4**, 1800589 (2019).

[3] W. Millar, *Some general theorems for non-linear systems possessing resistance*, The London, Edinburgh, and Dublin Philosophical Magazine and Journal of Science. **42**, 333 (1951).

[4] R. Kubo, *Statistical-mechanical theory of irreversible processes. I. General theory and simple applications to magnetic and conduction problems*, J. Phys. Soc. Jpn. **12**, 570 (1957).

[5] Z. Biolek, D. Biolek, and V. Biolková, *Interpreting area of pinched memristor hysteresis loop*, Electron. Lett. **50**, 74 (2014).

[6] L. Chua, *Memristor-The missing circuit element*, IEEE Trans. Circuit Theory **18**, 507 (1971).

[7] D. B. Strukov, G. S. Snider, D. R. Stewart, and R. S. Williams, *The Missing Memristor Found*, Nature **453**, 80 (2008).

[8] Y. V. Pershin, and M. Di. Ventra, *A simple test for ideal memristors*, Journal of Physics D: Applied Physics, **52**, 1 (2018).

[9] S. Park, H. Jeong, J. Park, J. Bae, and S. Choi, *Experimental demonstration of highly reliable dynamic memristor for artificial neuron and neuromorphic computing*, Nat Commun **13**, 2888 (2022).

[10] J. Borghetti, G. S. Snider, P. J. Kuekes, J. J. Yang, D. R. Stewart, and R. S. William, *"Memristive" switches enable "stateful" logic operations via material implication*, Nature **464**, 873 (2010).

[11] Z. Wang *et al.*, *Memristors with diffusive dynamics as synaptic emulators for neuromorphic computing*, Nat. Mater. **16**, 101 (2017).

[12] Y. Li, Z. Wang, R. Midya, Q. Xia, and J. J. Yang, *Review of memristor devices in neuromorphic computing: materials sciences and device challenges*, J. Phys. D: Appl. Phys. **51**, 503002 (2018).

[13] F. M. Bayat, F. M. Bayat, M. Prezioso, B. Chakrabarti, H. Nili, I. Kataeva, and D. Strukov, *Implementation of multilayer perceptron network with highly uniform passive memristive crossbar circuits*, Nat. Commun. **9**, 2331 (2018).

[14] Z. Wang *et al.*, *Reinforcement learning with analogue memristor arrays*, Nat. Electron. **2**, 115 (2019).
[15] Z. Liu *et al.*, *Neural signal analysis with memristor arrays towards high-efficiency brain-machine interfaces*, Nat. Commun. **11**, 4234 (2020).
[16] M. Lanza, et al. *Memristive technologies for data storage, computation, encryption, and radio-frequency communication* Science. **376**, 6597(2022).
[17] A. Sebastian, M. Le Gallo, R. Khaddam-Aljameh, and E. Eleftheriou, *Memory devices and applications for in-memory computing*, Nat. Nanotechnol. **15**, 529 (2020).
[18] S. J. Kim, S. Kim, and H. W. Jang, *Competing memristors for brain-inspired computing*, iScience **24**, 101889 (2021).
[19] S. Kundu, P. B. Ganganiak, J. Louis, H. Chalamalasetty, and B. P. Rao, *Memristors Enabled Computing Correlation Parameter In-Memory System: A Potential Alternative to Von Neumann Architecture*, IEEE Trans. VLSI Syst. **30**, 755 (2022).
[20] P. Pfeiffer, I. L. Egusquiza, M. Di Ventra, M. Sanz, and E. Solano, *Quantum Memristors*, Sci. Rep. **6**, 29507 (2016).
[21] S. N. Shevchenko, Y. V. Pershin, and F. Nori, *Qubit-Based Memcapacitors and Meminductors*, Phys. Rev. Appl. **6**, 014006 (2016).
[22] S. N. Shevchenko and D. S. Karpov, *Thermometry and Memcapacitance with a Qubit-Resonator System*, Phys. Rev. Appl. **10**, 014013 (2018).
[23] S. Peotta and M. Di Ventra, *Superconducting Memristors*, Phys. Rev. Appl. **2**, 034011 (2014).
[24] J. Salmilehto, F. Deppe, M. Di Ventra, M. Sanz, and E. Solano, *Quantum Memristors with Superconducting Circuits*, Sci. Rep. **7**, 42044 (2017).
[25] M. Sanz, L. Lamata, and E. Solano, *Quantum Memristors in Quantum Photonics*, APL Photonics **3**, 080801 (2018).
[26] T. Gonzalez-Raya, J. M. Lukens, L. C. Céleri, and M. Sanz, *Quantum Memristors in Frequency-Entangled Optical Fields*, Materials **13**, 864 (2020).
[27] M. Spagnolo, J. Morris, S. Piacentini, M. Antesberger, F. Massa, F. Ceccarelli, A. Crespi, R. Osellame, and P. Walther, *Experimental photonic quantum memristor*, Nat. Photon. **16** 318–323 (2022).
[28] D. Marković and J. Grollier, *Quantum neuromorphic computing*, Appl. Phys. Lett. **117**, 150501 (2020).
[29] K. Fujii and K. Nakajima, *Harnessing Disordered-Ensemble Quantum Dynamics for Machine Learning*, Phys. Rev. Applied, **8**, 024030 (2017).
[30] K. Fujii and K. Nakajima, *Quantum Reservoir Computing: A Reservoir Approach Toward Quantum Machine Learning on Near-Term Quantum Devices*, Natural Computing Series, Springer, Singapore, 423–450 (2021).
[31] S. Kumar, F. A. Cárdenas-López, N. N. Hegade, X. Chen, F. Albarrán-Arriagada, E. Solano, and G. A. Barrios, *Entangled quantum memristors*, Phys. Rev. A **104**, 062605 (2021).
[32] S. Kumar, F. A. Cárdenas-López, N. N. Hegade, F. Albarrán-Arriagada, E. Solano, and G. A. Barrios, *Tripartite entanglement in quantum memristors*, Phys. Rev. Applied **18**, 034004 (2022).
[33] L. O. Chua and S. M. Kang, *Memristive devices and systems*, Proc. IEEE. **64**, 209 (1976).
[34] M. Di Ventra and Y. V Pershin, *On the physical properties of memristive, memcapacitive and meminductive systems.*, Nanotechnology, **24**, 255201 (2013).
[35] R. Kubo, *Statistical-mechanical theory of irreversible processes. I. General theory and simple applications to magnetic and conduction problems.*, J. Phys. Soc. Jpn, **12**, 570 (1957).
[36] I. Besedin, and A. P Menushenkov *Quality factor of a transmission line coupled coplanar waveguide resonator*, EPJ Quantum Technol. **5**, 2 (2018).
[37] R. Vijay, C. Macklin, D. H. Slichter, S. J. Weber, K. W. Murch, R. Naik, A. N. Korotkov, and I. Siddiqi, *Stabilizing Rabi oscillations in a superconducting qubit using quantum feedback*, Nature **490**, 77–80 (2012).
[38] G. de Lange, D. Risté, M. J. Tiggelman, C. Eichler, C. Eichler, L. Tornberg, G. Johansson, A. Wallraff, R. N. Schouten, and L. DiCarlo, *Reversing Quantum Trajectories with Analog Feedback*, Phys. Rev. Lett. , **112**, 080501 (2014).
[39] S. Lloyd and J. J. E. Slotine, *Quantum feedback with weak measurements*, Phys. Rev. A **62**, 012307 (2000).
[40] R. Johansson, G. Johansson, C. M. Wilson, and F. Nori, *Dynamical Casimir effect in superconducting microwave circuits*, Phys.Rev. A **82**, 052509 (2010).
[41] C. M. Wilson, G. Johansson, A. Pourkabirian, M. Simoen, J. R. Johansson, T. Duty, F. Nori, and P. Delsing, *Observation of the dynamical Casimir effect in a superconducting circuit*, Nature **479**, 376(2011).
[42] M. Di Ventra, Y. V. Pershin, and L. O. Chua, *Circuit Elements With Memory: Memristors, Memcapacitors, and Meminductors*, Proceedings of the IEEE, **97**, 10 (2009).
[43] K. B. Möller, T. G. Jörgensen, and J. P. Dahl, *Displaced squeezed number states: Position space representation, inner product, and some applications*, Phys. Rev. A. **54**, 5378(1996).
[44] B. Xiong, X. Li, S. L. Chao, Z. Yang, W. Z. Zhang, and L. Zhou *Generation of entangled Schrödinger cat state of two macroscopic mirrors*, Opt. Express **27**, 13547-13558 (2019).
[45] H. Ollivier and W. H. Zurek, *Quantum Discord: A Measure of the Quantumness of Correlations*, Phys. Rev. Lett. **88**, 017901 (2002).
[46] S. Luo, *Quantum discord for two-qubit systems*, Phys. Rev. A **77**, 042303 (2008).
[47] Online documentation scipy.optimize.basinhopping
[48] C. E. López, G. Romero, F. Lastra, E. Solano, and J. C. Retamal, *Sudden Birth versus Sudden Death of Entanglement in Multipartite Systems*, Phys. Rev. Lett. **101**, 080503 (2008).
[49] J. Yu, J. C. Retamal, M. Sanz, E. Solano, and F. Albarrán-Arriagada, *Superconducting circuit architecture for digital-analog quantum computing*, EPJ Quantum Technology **9**, 9 (2022).
[50] A. Blais, A. L. Grimsmo, S. M. Girvin, and A. Wallraf, *Circuit quantum electrodynamics*, Rev. Mod. Phys. **93**, 025005 (2021).
[51] J. Q. You and F. Nori, *Atomic physics and quantum optics using superconducting circuits*, Nature. **474**, 589-597 (2011).
[52] X. Gu, A. F. Kockum, A. Miranowicz, Y. Liu, and F. Nori, *Microwave photonics with superconducting quantum circuits*, Physics Reports. **718–719**, 1-102 (2017).

[53] R. Assouly, R. Dassonneville, T. Peronnin, A. Bienfait, and B. Huard, *Demonstration of Quantum Advantage in Microwave Quantum Radar*, arXiv:2211.05684 (2022).